Fabrication of Two Different Probe Architectures for Ultra-Compact Image Sensors for Root Canal Observations

Masataka Fujimoto[1], Shinji Yoshii[1], Satoshi Ikezawa[2], Toshitsugu Ueda[2], and Chiaki Kitamura[1]
1. Div. of Endodontics and Restorative Dentistry
Kyushu Dental University, Japan
2. Graduate School of Information, Production and Systems
Waseda University, Japan

***Abstract*—With the development of dental instruments such as dental microscopes and cone beam computed tomography (CBCT), the precision of current dental diagnosis and treatment has greatly improved. However, the observation of deep periodontal pockets, fractures near the root apex, and collaterals of root canals is difficult using these instruments. To solve these problems, we developed two types of micro-image sensors that can be used for the observation of root canals. The first image sensor is an external-irradiation probe that uses an external light source. This probe has high-resolution and a wide field of view. The other sensor is an internal-irradiation probe, which can be used to observe an image and transmit the illumination light with a single probe. The external-irradiation probe has an image fiber with a diameter of 600 µm and a gradient index (GRIN) lens. The internal-irradiation probe has an image fiber with a diameter of 300 µm, a GRIN lens, and 40 optical fibers with a diameter of 40 µm each as a light source. Using these probes, we captured the image of a resolution chart; line spaces with widths of 10 to 100 µm were observed using both types of probes. The evaluations of the visibility of the captured image showed higher measurement values than those of commercially available endoscopes. We will apply this ultra-compact image sensor to various fields besides dentistry, such as medical and industrial applications.**

***Index Terms*— endoscope, GRIN lens, image fiber, root canal**

I. Introduction

TEETH are the hardest tissue in the human body and have numerous fine structures as shown in Fig. 1.

Fig. 1 (a) shows the cross-sectional view of the human tooth, which includes hard tissue called enamel that is harder than bone or dentin. Soft tissue called dental pulp that includes a combination of nerves and blood vessels is also contained inside the teeth. As a marked structure of a tooth, canals including thin pulp, called root canals, exist in each tooth root. Dental caries (Figs. 1 (a, b)), a common disease observed in a tooth, sometimes damages dental pulp, and dentists eventually remove whole dental pulp, to relieve patients from serious pain. In the field of dentistry, a dentist is forced to treat root canal and deep periodontal pocket blindly without visual corroboration. While performing a surgical procedure such as the treatment of deep periodontal pockets, the affected area can be viewed; however, the surgical treatment places a large burden on the patient, and cannot be applied to all patients. On the other hand, when dental caries reach the dental pulp, and the bacterial infection reaches the periodontal tissue at the apex, endodontic treatment is necessary [1]. Specifically, in endodontic treatment, dental pulp and materials causing the bacterial infection are removed from the root canal. First, the dentist cuts away the dental caries with a machine called an air turbine. After all the caries are removed, the unnecessary parts of tooth crown are also removed to view the entrance of the root canal more clearly. Then, all the dental pulps of the root canal are removed and the root canals are washed with a cleaning solution. The entrance of the root canal is very small and has a complicated shape; in most cases, dentists operate using an instrument and perform the treatment blindly [2-4].

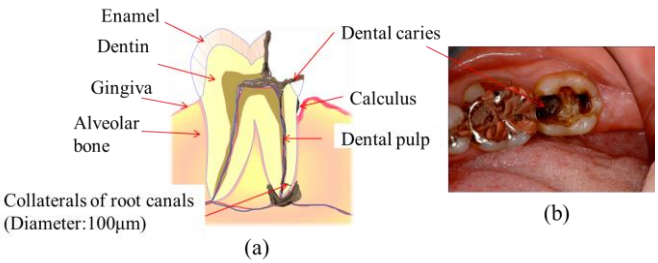

Fig. 1. (a) Cross-sectional view of the human tooth and (b) photograph of the dental caries

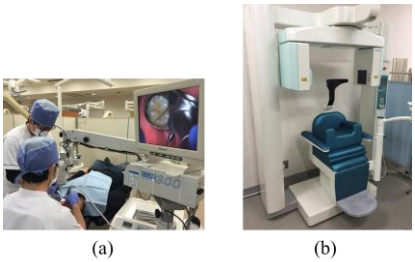

Fig. 2. Developed dental instruments (a) dental microscope, (b) CBCT

By using the recently developed dental microscopes, dentists can observe the fractures and narrowed root canal, which were previously difficult to observe and treat [5,6]. Furthermore, after the development of cone beam computed tomography (CBCT), three-dimensional (3D) diagnosis of the range of periapical lesions, which were difficult to observe in dental X-ray photographs, also became possible [7-10]. However, even when using these instruments, the observation of collaterals of the root canals and fractures near the apex is still difficult. By using a dental microscope, dentists can see near the entrance of the root canal; however, CBCT cannot be used to observe fine structures, as it does not have a high resolution.

To solve the aforementioned problems, a new endoscope, which allows observation inside the periodontal pocket and root canals with high-resolution, is required. We considered using fiber endoscopes because they have a small diameter and are minimally invasive [11-14]. However, most prior dental research on endoscopes involved periodontal pockets [15-17]. In contrast, a dental endoscope designed for the fine structures inside of the root canals is not yet commercially available. Commercially available endoscopes that have a smaller diameter do not have a suitable light distribution and the image resolution of approximately 3,000 pixels is insufficient for diagnosis and treatment.

For the reasons stated above, we have developed a dental endoscope that can be used to observe the fine structures of the root canal [18-20]. An image fiber bundled with a large number of single-mode fibers was used for the image transfer; it was developed through the application of various studies [21-23]. The specifications of the image fiber are: 15,000 pixels, 600 μm outer-diameter, and 500 mm length. The image was obtained using two methods. In the first method, the illumination light was transmitted outside the image fiber; in the second method, the illumination traveled inside of the image. As a result, lines and spaces with widths of 10, 20, 50, and 100 μm were observed using both methods; however, the observation was not possible unless the tip of the endoscope touched the samples.

In this study, we added a lens to our previous endoscope system so that observations could be performed without touching the samples [18-20]. We fabricated two prototypes—with distinct designs—to solve the aforementioned problems of the current endoscopes. First, we fabricated an external-irradiation system with an illumination light outside of the probe. This system had a 15,000-pixel image fiber and a GRIN lens. We obtained high-resolution images on the resolution chart. However, observations were not possible unless the probe end touched the sample. Therefore, we designed another system—the internal-irradiation system. This system was used to illuminate the observation area and capture the images with a single endoscope probe. Furthermore, we designed a new GRIN lens to extend the object working distance. The internal-irradiation system comprised the image fiber, the GRIN lens, and the optical fibers for the light source. Optical fibers were placed around the image fiber. To further facilitate the insertion of the probe into the root canal, the diameter of the image fiber was selected to be thinner than that of the external-irradiation system to reduce the overall diameter of the probe. The new GRIN lens was designed, taking into consideration factors such as the magnification, the pitch of the GRIN lens, the working distance, and the light utilization efficiency.

This paper reports on the design methods and evaluation of our endoscope.

II. Experimental Setup

Fig. 3 shows the final image of the endoscope system. This system consists of a PC, complementary metal oxide semiconductor (CMOS) sensor, objective lens, and probe. The

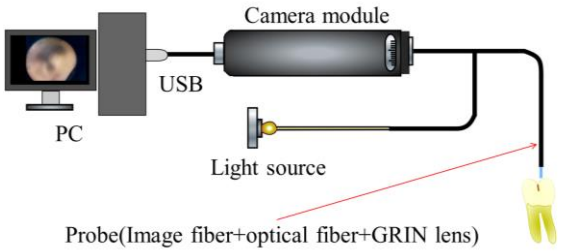

Fig. 3. Our endoscope system

image of the target is transmitted in real-time from the CMOS sensor to the PC on the opposite end of the image fiber, where it is displayed on the monitor of the PC. This CMOS sensor has full-color capability, a 2-megapixel lens, and video capture capability. The specifications of the probe are given in the next section.

A. Gradient-index (GRIN) lens

The GRIN lens is a cylindrical lens and utilizes many microscopes. The shape of the GRIN lens is simple and it is easy to use in an optical system with low fabrication cost. GRIN lenses have been used in various medical devices such as endoscopes and microscopes [24-28]. We describe the basic imaging method of the GRIN lens: The GRIN lens has a gradient refractive index and the refractive index is the highest at the center axis of the lens. Therefore, the light rays inside the

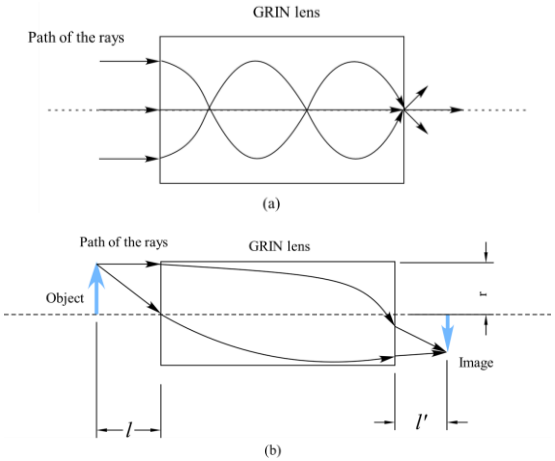

Fig. 4. (a) Path of the rays in a medium with a quadratic index variation, (b) imaging using the GRIN lens

GRIN lens follow a curve that is based on the gradient of the refractive index as shown in Fig. 4 (a). The schematic diagram

of the imaging of the GRIN lens is shown in Fig. 4 (b). In this figure, *l* is the object working distance, *l'* is the image working distance, and *r* is the radius of the GRIN lens.

Imaging in the GRIN lens is described by the following equations [29-31]:

$$N(r) = n_0(1 - \frac{\sqrt{A}^2}{2} r^2) \quad (1)$$

In (1), where n_0 is the refractive index of the medium on the cylindrical axis, $\sqrt{A}$ is the refractive-index-distribution constant, and r is the radius of the cylinder of the GRIN lens. The light enters into the GRIN lens in the form of a curve and exits from the other end face. While the light travels through the lens, the ray propagates in a meandering sinusoidal path. The length of the wave for one period is defined as the pitch of the GRIN lens. The working distance of the GRIN lens can be changed by changing the pitch of the lens, and the pitch of the GRIN lens depends on the length of the lens. The relationship between the length of the lens and the pitch can be expressed as follows:

$$Z = \frac{2\pi P}{\sqrt{A}} \quad (2)$$

where Z is the length of the GRIN lens and P is the pitch of the GRIN lens.

Table I shows the equations for the GRIN lens. For imaging using the GRIN lens, the relationship between the object working distance l, which is the distance between the object and the surface of the GRIN lens, and the image working distance l', which is the distance between the image and the opposite surface of the GRIN lens, is shown in the equation in Table I; the equations for magnification M and numerical aperture $N.A._{GL}$ are also shown.

TABLE I. EQUATIONS OF THE GRIN LENS

Image working distance (l')	$l' = \frac{1}{n_0\sqrt{A}} \cdot \frac{n_0 l\sqrt{A}\cos(2\pi P) + \sin(2\pi P)}{n_0 l\sqrt{A}\sin(2\pi P) - \cos(2\pi P)}$
Magnification (M)	$M = \frac{1}{\cos(2\pi P) - n_0 l\sqrt{A}\sin(2\pi P)}$
Numerical Aperture ($N.A._{GL}$)	$N.A._{GL} = \sin\theta = \sqrt{n_0^2 - n_r^2}$

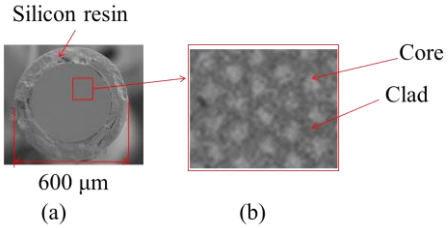

Fig. 5. Image fiber (a) cross section of the image fiber, (b) cores and clads

B. *Image fiber*

In this experiment, the image fibers used were multi-core fibers with a many small-diameter (4 μm) cores in a single fiber. An image fiber can transmit an image to the end surface of the fiber from the opposite surface. The image of the cross section of the image fiber is shown in Fig. 5(a). The center area is the imaging area, and it is covered with a silicon resin. In Fig. 5(b), the core of the image fiber light-gray areas, and darker gray areas are the clad of the fiber bundle.

The outermost layer of the image fiber is covered with a silicone resin and the image acquisition area is coated with acrylate resin and a quartz jacket.

C. *System construction*

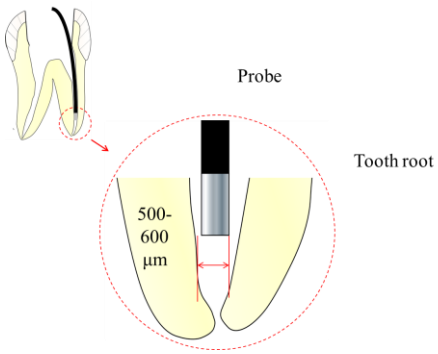

Fig. 6. Model of the root canal and probe

Considering the requirements for the prototype of an endoscope, the diameter and resolution of the probe are important factors to be considered. Fig. 6 shows the illustration of the root canal model.

Dentists perform root canal treatment at approximately 500 to 600 μm from the apical portion of the root canal. The entrance of the root canal is around 1 mm in diameter and, since they insert the probe inside the root canal, the diameter of the probe must be smaller than 600 μm. Next, we consider the resolution requirements of our endoscope. The diameter of the collaterals and the width of fractures are typically 50-100 μm. The diameter of the core in the image fiber is 4 μm. For observing through the naked eye, we need 4-pixel images and therefore, the desirable resolution should be higher than 12-25 μm.

1) *External-irradiation system*

In our previous study, we fabricated an endoscope using only an image fiber. However, the endoscope could not be used to observe the sample without touching the sample. Therefore, we considered including a GRIN lens for the observation. First, we show the specifications of the image fiber used in the probe for the external-irradiation system in Table II.

TABLE II. SPECIFICATION OF THE IMAGE FIBER IN EXTERNAL-IRRADIATION SYSTEM

Number of cores	15,000 pixels
Diameter of imaging area	500±20 [μm]
Diameter of fiber	500±20 [μm]
Diameter of jacket	600±30 [μm]
Minimum bending radius	30 [μm]
Distance between cores	3.38 [μm]

The image fiber used in this study has 15,000 cores and is 500 μm in diameter; the distance between the cores is 3.38 μm. The jacket of the fibers was removed with acetone to reduce the probe diameter. The image fiber was used by attaching the lens with a UV curing adhesive. Table III shows the specifications of our GRIN lens. In this case, the image working distance *l'* was effectively 0.0 mm and the pitch was 0.25 λ. The GRIN lens used in this system has the same diameter as the imaging area of the image fiber to facilitate the fabrication. This lens has a magnification of 1.

TABLE III. SPECIFICATION OF THE GRIN LENS IN THE EXTERNAL-IRRADIATION SYSTEM

Diameter of GRIN lens	500 [μm]
Image working distance	0.0 [mm]
Pitch	0.25 λ
Magnification	1

Fig. 7 (a) shows the schematic diagram of the endoscope with the external-irradiation system. The image fiber and GRIN lens were bonded inside the metal tube using ultraviolet (UV) curable adhesive as shown in Fig. 7 (b), and unnecessary bubbles were removed.

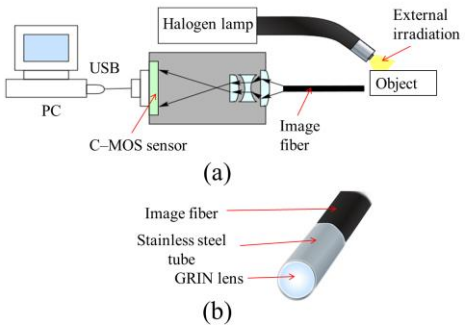

Fig. 7. (a) The endoscope with an external-irradiation system, (b) illustration of the probe in the external-irradiation system

2) Internal-irradiation system

We fabricated the external-irradiation system with the object working distance of 0.0 mm that is similar to that of the image fiber. During a root canal procedure, using an object working distance of 0.0 mm probe is difficult because of the bends of the root canals. Therefore, we considered an optimized object working distance to change the pitch of the GRIN lens. Moreover, illumination light does not reach the root canals properly; we attempted to obtain the illumination light with a single probe.

a) Design of GRIN lens

This system can be used to obtain the image and the illumination light. We used ultra-thin optical fiber for the illumination light; image fiber with a smaller diameter was used to place the optical fibers. Table IV shows the specifications of the image fiber in the internal-irradiation system. The image fiber used in this system has a diameter of 300 μm for the imaging area, and the number of cores equals 6,000 pixels. To accommodate such a large number of optical fibers, we used small diameter image fiber in this probe. The distance between the cores is 3.38 μm, and in the PC monitor, a minimum of 2 pixels are necessary for observation.

TABLE IV. SPECIFICATION OF THE IMAGE FIBER IN INTERNAL-IRRADIATION SYSTEM

Number of cores	6,000 pixels
Diameter of imaging area	270±20 [μm]
Diameter of fiber	300±20 [μm]
Diameter of jacket	400±30 [μm]
Minimum bending radius	30 [μm]
Distance between cores	3.38 [μm]

For naked eye observation, 4 pixels are required and for an ideal observation, 10 pixels are required. For this reason, the size of the objective image should be 12-16 μm at the surface of the image fiber for naked eye observation. The observation of fine targets, such as the collaterals of the root canals and fractures, requires 50 μm; the requirements of the internal-irradiation system are shown in Table V.

TABLE V. REQUIREMENTS OF THE INTERNAL-IRRADIATION SYSTEM

Parameter	Minimum	Ideal
Objective length	50 [μm]	
Pixels	4	10
Image length	13.52 [μm]	33.8 [μm]
Magnification	0.27	0.68

The second and third columns of this table show minimum and ideal requirements, respectively.

Here, the magnification of the GRIN lens is shown below.

$$M = \frac{1}{\cos(2\pi P) - n_0 l\sqrt{A}\sin(2\pi P)} \quad (3)$$

From this equation, l can be represented by the following equation.

$$l = \frac{\cos(2\pi P) - \frac{1}{M}}{n_0 l\sqrt{A}\sin(2\pi P)} \tag{4}$$

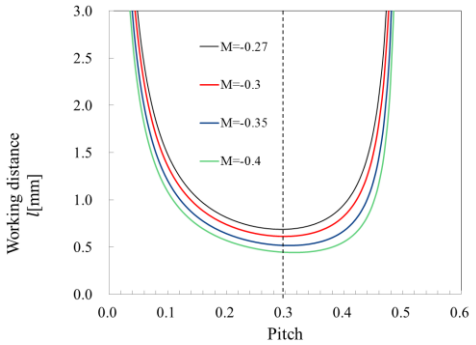

Fig. 8. Calculated relation for variation of the M between the image working distance and the pitch of the GRIN lens

Fig. 8 represents the relation between the image working distance and the pitch of the GRIN lens in the form of a graph.

From the graph, it can be seen that the image working distance decreases as the magnification increases. Consequently, the magnification of the GRIN lens was set to be 0.27.

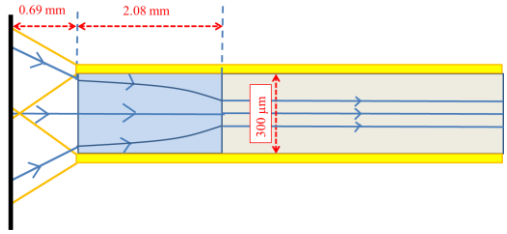

Fig. 9. Calculated relation of the image working distance and the pitch of the GRIN lens

Next, we consider how the illumination light can be efficiently used. Fig. 9 shows the construction of the probe. In this figure, Z is the irradiation range obtained from the optical fiber for the light source and H is the viewable range by the image fiber. Moreover, α and θ denote the maximum angle with respect to the optical axis of the emitted light for the GRIN lens and optical fiber, respectively. The numerical aperture of the GRIN lens $N.A._{GL}$ and optical fiber $N.A._{OF}$ used in this experiment are 0.65 and 0.37, respectively. Here, H can be represented by the following equation.

$$\begin{aligned} H &= \frac{D_{IF}}{M} \\ &= D_{IF}(\cos(2\pi P) - n_0 l\sqrt{A}\sin(2\pi P)) \end{aligned} \tag{5}$$

In addition, Z can be represented as follows.

$$\begin{aligned} Z &= 2l\tan\theta + D_{probe} \\ &= 2l\tan(\sin^{-1}(N.A_{OF})) \end{aligned} \tag{6}$$

Using the ratio of the field of view and the irradiation range of the illumination light, the efficiency of light η can be represented as follows.

$$\begin{aligned} \eta &= \frac{H^2}{Z^2} \\ &= \frac{D_{IF}{}^2(\cos(2\pi P) - n_0 l\sqrt{A}\sin(2\pi P))^2}{(2\tan(l\sin^{-1}(N.A_{OF}) + D_{probe})^2} \end{aligned} \tag{7}$$

The relation between the image working distance and the efficiency of the light is presented in the graph shown in Fig. 10. The part of η that has 1 or more values in the graph shows that the irradiation light by the optical fibers cannot reach the imaging area.

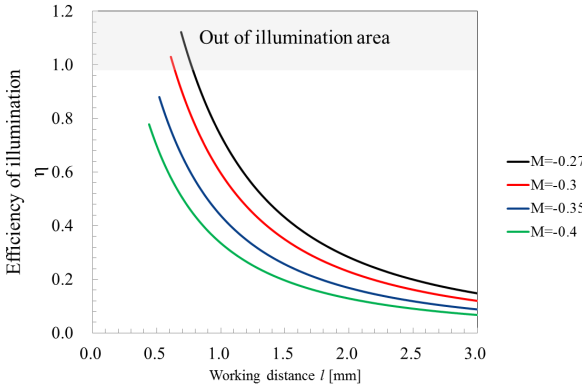

Fig. 10. Calculated relation between the image working distance and the pitch of the GRIN lens

From the above results, we finalized the design of the GRIN lens to obtain the highest efficiency of illumination light and a range that satisfies the resolution. Moreover, the image working distance is 0 mm. Therefore, the GRIN lens designed has a magnification of 0.27, a pitch of 0.29 λ, and an object working distance of 0.69 mm.

b) Specification of the light source

We used an LED as the light source in previous system [18-20]. Table VI shows the specifications of the LED light and Fig. 8 shows the relationship between the measured wavelength and the intensity of the LED. An LED was used as the light source because it can emit a sufficient amount of light and causes no harm to the human body [32-34]. The peak of the wavelength was found to be 450 nm from the graph showing the relationship between the wavelength and the intensity.

TABLE VI. SPECIFICATION OF LED LIGHT SOURCE

Type	OSW4XME3C1S
Size	19.9 [mm]
Deg	120
Color	Pure white
Lens	Yellow diffused
Voltage	3.3 [V]
Intensity	200 [lm]

Table VII shows the specifications of the fiber was used. The optical fiber for the light sources had a core diameter of 30 μm and numerical aperture of 0.22. The optical fiber was in direct

contact with the LED light source and the illumination light was transmitted. The measured average illumination light emitted from the fiber tip was 0.24 μW for a single fiber. Using 40 fibers in the probe, we obtained a total illumination light intensity of 10 μW.

TABLE VII. SPECIFICATIONS OF THE OPTICAL FIBER

Diameter of core	30±20 [μm]
Diameter of clad	35±20 [μm]
Diameter of jacket	40±30 [μm]
Numerical Aperture	0.22

c) Design of the internal-irradiation probe

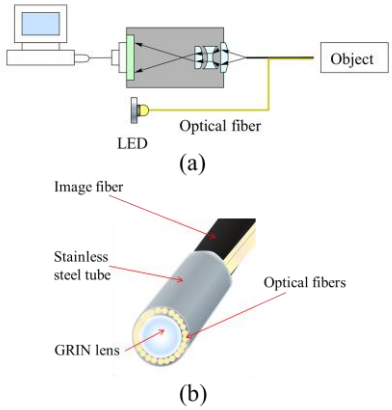

Fig. 11. (a) Endoscope with the internal-irradiation system, (b) illustration of the probe in the internal-irradiation system

In this section, we describe the design of the probe in the internal-irradiation system.

Fig. 11. (a) shows the schematic diagram of the internal irradiation system. This system can obtain images and produce the illumination light through a single probe.

The light emitted from the surface of the sample passes through based on the pitch of the GRIN lens; it is emitted to the image fiber. The GRIN lens and the image fiber are bonded to each other using a UV curing adhesive. The distance from the lens surface and the objective surface represents the object working distance. The construction of the probe tip is shown in Fig. 11 (b). The endoscope probe was constructed with the image fiber, optical fibers, and the GRIN lens. The pitch of the GRIN lens, 0.29 λ, is too short to manipulate; hence, to facilitate the operation, the pitch of the GRIN lens was extended by 0.5 λ and the final pitch of GRIN lens was 0.79 λ. In this case, extending the pitch by 0.5 λ reverses only the direction of the image and there is no change in the size of the image formed. The length of the final GRIN lens was 2.08 mm.

In addition, the probe was fabricated with a jig for coupling the image fiber and the GRIN lens. The GRIN lens and the image fiber were put on stages that were capable of fine position adjustment; after attaching these materials, we used a microscope for fine operation. After bonding the GRIN lens and the image fiber to the optical fiber for the light source, they were coated with a stainless steel tube. Each material was coated with a UV curing adhesive and irradiated with UV for 15 min for each step.

III. RESULTS

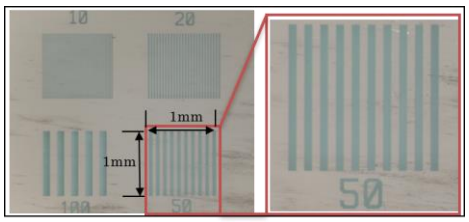

Fig. 12. Resolution chart

We used a resolution chart same as previous research [18-20], shown in Fig. 12, for experimental observations using our endoscope systems. The resolution chart used in the experiments was glass, patterned with a Cr thin film. In addition, the resolution chart had a grid-pattern with lines and spaces drawn every 10, 20, 50, and 100 μm, which was used as an observation sample. These patterns were drawn by a focused ion beam technique.

A. *External-irradiation system*

1) *Obtaining the image*

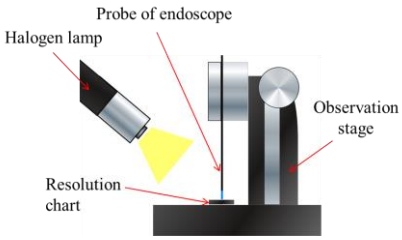

Fig. 13. Illustration of the observation system

The fabricated endoscope probe was mounted on a stage capable of fine position adjustment as shown in Fig. 13. We mounted the resolution chart on the observation stage and held the probe in a fixed position. In this stage, the probe can move along one axis. The resolution chart was illuminated by a halogen lamp. As described in the previous section, we fabricated the external-irradiation system and observed the resolution chart. Fig. 14 shows the observation results of our

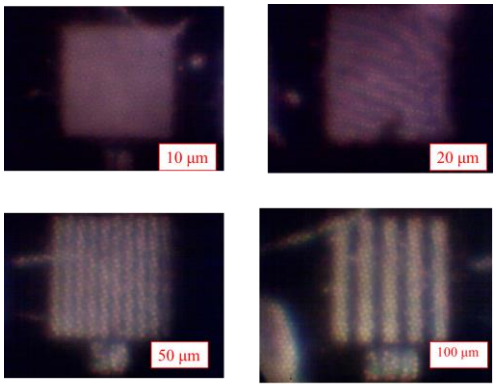

(a)

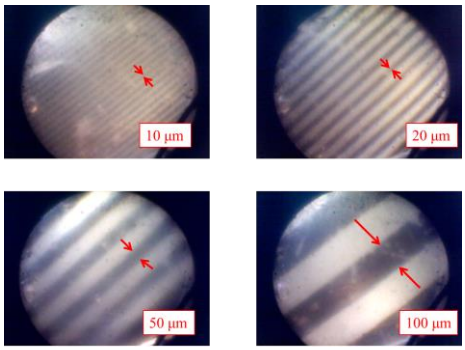

Fig. 14. Obtained images with (a) commercially available endoscope (b) and our endoscope with the internal-irradiation system

external-irradiation system and those of the commercially available endoscope. We observed the 10, 20, 50, and 100 μm lines and spaces of the resolution chart. The image of the commercially available endoscope is acceptable for 50 and 100 μm widths of the lines and spaces; however, the 10 and 20 μm lines and spaces are not clearly visible. On the other hand, the image of our endoscope system can be observed for all widths of the lines and spaces. Compared with commercially available

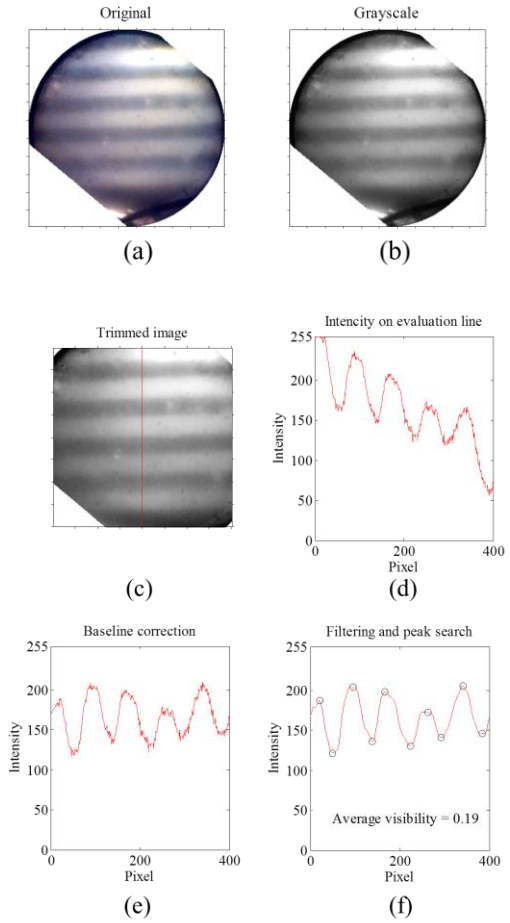

Fig. 15. Evaluation of the visibility: (a) Rotated original image, (b) Grayscale image, (c) Trimming and drawing a line, (d) Original measuring value, (e) Baseline correction, (f) Smoothing and peak searching

endoscopes, our system is capable of clear observations with the naked eye. Observations showed that in the images obtained using our endoscope, the tip of the probe was almost touching the surface of the resolution chart.

2) Evaluation of the image

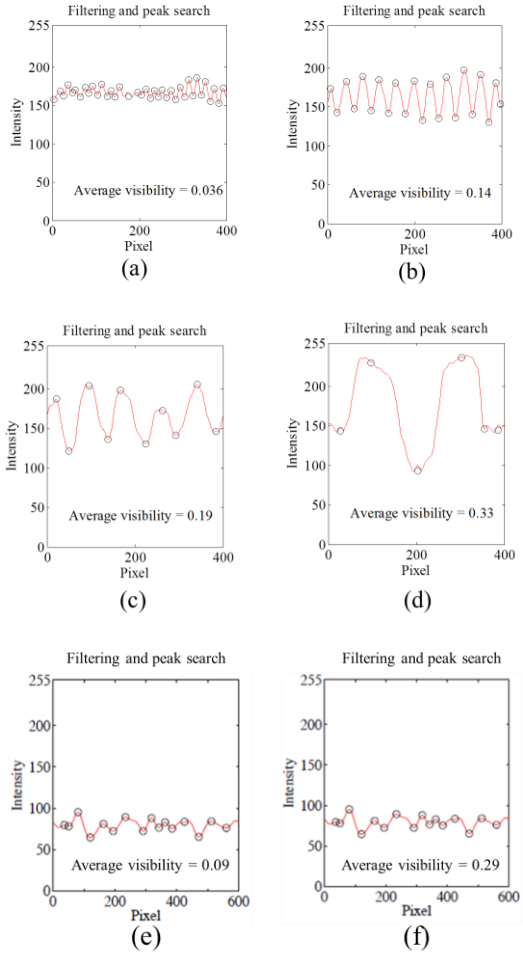

Fig. 16. Evaluation of each image. (a-d): our endoscope; 10, 20, 50, and 100 μm, (e,f): commercially available endoscope; 50 and 100 μm

For quantitative evaluation of the captured images, we evaluated the visibility of each image. For the evaluation, the captured images were rotated as their lines parallel to horizontal axis, and the images were converted to grayscale images. The center square of 400 × 400 pixels of the image was cut out. In Fig. 15, vertical red lines are shown at the center of the image representing the grayscale value of each pixel in the graph. Halation was also observed in the acquired image. In order to solve the halation problem, a slope correction was applied to the graph, and the result was approximated using a low-pass filter. We substituted the local maximum and minimum values of the final graph as follows.

$$Visibility = \frac{I_{max} - I_{min}}{I_{max} + I_{min}} \quad (8)$$

where I_{max} and I_{min} are the local maximum and minimum of the intensity on the finished graph, respectively. Fig. 16 (a-d) shows the final graph of the each image when using our

endoscope system. The graph of the commercially available endoscope is shown in Fig. 16(e-f). Comparing our endoscope to the commercially available model, the variation of the graph (a-d) is more uniform than the variation of the graph (e-f). These results demonstrate that our endoscope can capture image efficiently.

B. *Internal-irradiation system*

1) Evaluation of the light intensity

We measured the amount of light radiated from the tip of the probe in the internal-irradiation system with a power sensor. The variation of the illumination light is converted to a voltage output of 0.5 V/mW. We obtained the illumination light with the probe and the light was converted into electric signals. We noted the voltage at the sensor, and then calculated the illuminance. The measured result of the illuminance was 4.6 μW. This result indicates that the light transmitted through a single optical fiber for a light source is less at the distal end.

2) Obtaining the image

The internal-irradiation system endoscope was fabricated using the aforementioned methods. Fig. 17 shows the finished probe.

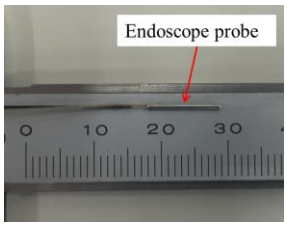

Fig. 17. Fabricated probe

The end of the fabricated probe was covered with a stainless steel tube. The outside diameter of the probe end was 830 μm. Using this probe, we observed the resolution chart. During the experiments, we positioned the probe on a stage capable of fine position adjustment. Fig. 18 shows the final captured images with our internal-irradiation system endoscope after measuring the optimal working distance. In these images, the cores of the image fiber can be confirmed, and the sharpest focus occurs at the left side and the central area. The edges of the images remain distorted because of the refractive index gradient. We could observe the 10, 20, 50, and 100 μm lines and spaces of the resolution chart with the internal-irradiation system. The transitions between the lines and the spaces are slightly blurred. Moreover, the captured images were clearer to the naked eye than those of the commercially available endoscope.

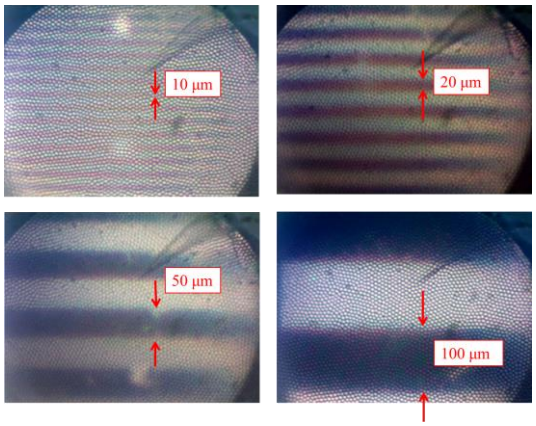

Fig. 18. Captured image with the internal irradiation probe

3) Evaluation of the image

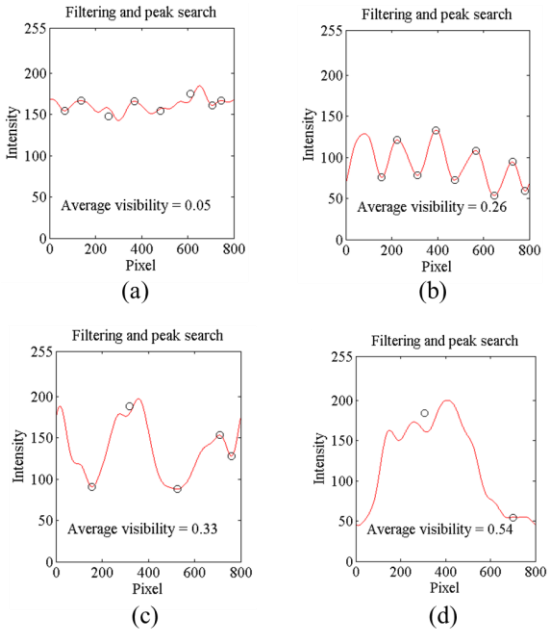

Fig. 19. Evaluation of the visibility for internal-irradiation probe: (a) 10 μm, (b) 20 μm, (c) 50 μm, (d) 100 μm

For a quantitative evaluation of the captured images, we evaluated the visibility of each image; the results are presented in Fig. 19. For the internal-irradiation system, the visibility increased as the width of the lines and spaces increased just as in the case of the external-irradiation system; however, higher values were obtained. We measured the visibility with by varying the object working distance at 0.01-mm intervals, and obtained a graph of the relationship between the working distance and visibility. Fig. 20 displays the results. In this graph, the high visibility area corresponds to a working distance value of 0.35-55 mm. The highest visibility (0.55) was obtained at a working distance of 0.32-033 mm.

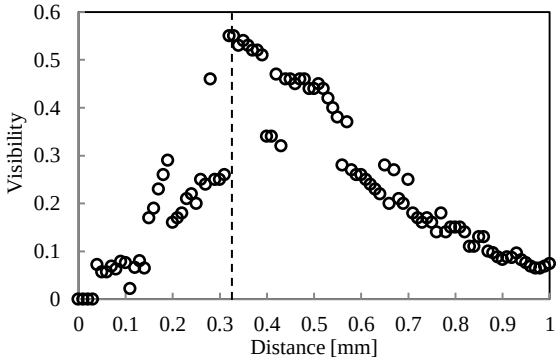

Fig. 20. Evaluation of the working distance

B. Observation of an actual human tooth

We observed actual human root canals in addition to the resolution chart. Fig. 21 (a) shows the schematic of the observation experiments for a human tooth using the micro probe. The human tooth observed in this experiment was a molar tooth that had been prepared for a root canal procedure. In Fig. 21 (b), we can observe the root canals and the isthmus between the root canals with our external-irradiation system probe. We attempted to capture the images with the internal-irradiation system; however, a clear image was not obtained, because the captured image did not have sufficient light illumination intensity and the working distance was too short to observe the root canal.

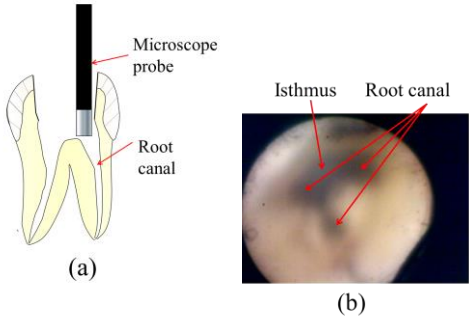

Fig. 21. (a) Illustration of observation, (b) obtained image for the observation of an actual human tooth

IV. Discussion

In this research, we developed two types of endoscopes, namely, the internal-irradiation system and the external-irradiation system probes. Our experiments showed that both of these endoscopes had higher resolution than commercially available endoscopes.

First, we describe the external-irradiation system. In our previous study, we fabricated an endoscope based only on the image fiber. However, the endoscope could not perform observations without touching the sample. Therefore, we considered adding the GRIN lens for conducting the observations. Our designed probe was attached to the end surface of the image fiber and the GRIN lens. We then used the GRIN lens with an image working distance of 0.0 mm. The fabricated probe end had a diameter of 600 μm, and the image fiber had 15,000 cores; using this we captured higher resolution images as compared to the internal-irradiation probe. The probe fabricated in this experiment could be used for observing the lines and spaces with a width of 10, 20, 50, and 100 μm on the resolution chart. Therefore, the prototype external-irradiation type probe can be used to obtain a desirable resolution for the observation. In addition, we analyzed the visibility of the images for each line and space, and found that the visibility value increased as the width of the lines and spaces increased.

Next, we describe the internal-irradiation system. The fabricated probe had no deviation about the optical axis of the GRIN lens and that of the image for obtaining the image. The tip of the probe was covered with a stainless steel tube, its endurance while inserting it in the root canal ensured. In addition, the total diameter of the probe was 830 μm. The boundary surface of the GRIN lens and the image fiber becomes unnecessarily thick when optical adhesive is used while attaching these materials. Hence, large diameter stainless steel tube should be used. We need to further reduce the diameter for ease of insertion into the root canals. In particular, the root canals of the molars have a smaller diameter than those of the incisal and premolar teeth. We need to design new methods for attaching the probe that can be used for all teeth. In the observation of an actual human tooth, we could not obtain images from inside the tooth. We used 40 optical fibers with a diameter of 40 μm each in order to secure the light intensity, but the amount of light was still less than the design value. When fabricating the endoscope for observing a wider field of view, larger diameter optical fibers should be used to extend the area of the illumination light. However, when using fibers with larger diameter, the number of fibers that can be used is reduced, or the diameter of the image fiber also has to be decreased. Therefore, when increasing the output of the light source to ensure sufficient amount of light, the propagation loss must be considered. In addition, no clear image of the actual human tooth was obtained because of the low contrast of the image. Inside the tooth, the entire wall of the root canal is white in color and we obtain only low contrast images. In the future, we will consider overlaying the different images obtained using different color light sources. The internal-irradiation system had desirable resolution. From the captured images, widths of 10, 20, 50, and 100 μm of the lines and spaces could be observed on the resolution chart. Our fabricated probe will be used for insertion into the root canals; the collaterals of the root canals and lines of tooth fractures will be observed. The expected diameter of the root canals and the width of the tooth fractures are approximately 100 μm and our internal-irradiation system achieves sufficient resolution to observe these. In addition, our captured images with the internal irradiation probe focus at the center of the image and the remaining parts of the images are distorted. The reason for this distortion is the gradient of the refractive index. Therefore, our probe has high accuracy because our fabricated endoscope can be observed fine specifications of the GRIN lens. We analyzed the visibility of the images for each line and space and observed that the visibility value increased as the width of the lines and spaces increased; the same phenomenon was observed in the external-irradiation system. The obtained working distance was shorter than the designed working distance for the GRIN lens. The short working distance was caused by the fact that the end surface of the GRIN lens was not positioned at the end of the probe at the adhesion step.

Comparing the two types of probes shown in Table VIII, the internal-irradiation probe has higher visibility; on the other hand, it is clear that with the external-irradiation system a wide-view image can be observed.

The internal-irradiation system shows higher visibility than the external-irradiation system; this is due to the addition of the objective lens between the CMOS sensor and the surface of the image fiber on the sensor side. The visibility value for the 10-μm-wide lines and spaces of for both probes was very small compared to other images. The probes are considered suitable for observing sizes in the range of 20-100 μm. To obtain higher resolution, the core diameter of the image fibers must be

smaller, and the number of cores must be increased. Currently, we can prepare an image fiber with a larger number of individual cores; however, the image fiber with a larger number of cores will inevitably have a larger diameter as long as the size of each core remains constant. To improve our probe, it is necessary to optimize the size of each component.

In addition, although the intensity of the illumination light has low power, the internal-irradiation system can obtain the illumination light by itself. When observing the periapical tissue, the observation of the fine structures is suitable because the illumination light is difficult to be obtained from the outside into the root canal. However, for observing the periodontal pockets and areas near the entrance of the root canal in a wide field of view, the external-irradiation system is suitable. Therefore, whether to use the internal-irradiation system or the external-irradiation system depends on what the dentist wants to observe.

TABLE VIII. COMPARING THE ENDOSCOPES

	Visibility			
	10	20	50	100
Commercial	-	-	0.09	0.29
External	0.036	0.14	0.19	0.33
Internal	0.05	0.26	0.33	0.54

We are also attempting to build 3D images using the acquired 2D images. In modern dentistry, 3D images are very useful for both clinical practice and research; and various studies have been conducted on 3D imaging [35]. Several prior studies have focused on the tooth and the bone of the jaw [36-39]. We constructed a 3D image using images that were acquired from the endoscope; however, constructing an accurate 3D image will be difficult until the image resolution is improved further.

In future work, we will attempt to improve our endoscope system such that it is capable of using a laser from the optical fiber for the light source. With such a device, dentists would be able to use the endoscope for dental treatment as well as for diagnosis. In addition, it could also be used for the diagnosis and treatment of blood vessels in the medical field.

V. CONCLUSION

In this research, we constructed two types of image sensors, one with an external-irradiation system and the other with an internal-irradiation system. Both types of endoscopes had a resolution of 10-100 μm based on the observations of the resolution chart. The internal-irradiation system could emit light with an intensity of 4.6 mW from the tip of the probe; however, the actual dental observation was difficult. We need to perform further improvements in the image resolution, obtain a stable amount of light, and design accurate observations of an actual human tooth.

ACKNOWLEDGEMENT

The authors would like to thank Mr. Tsuno, Dr. Zimin, Mr. Oigawa, and the master thesis students in the Graduate School of Information, Production and Systems, Waseda University and also Mr. Hang and Mr. Zhou for their support and direction for this study.

REFERENCES

[1] F. J. Vertucci, "Root canal morphology and its relationship to endodontic procedures," *Endod. Topics*, vol. 10, pp. 3–29, 2005.

[2] F. J. Vertucci, "Root canal anatomy of the human permanent teeth," *Oral. Surg. Oral. Med. Oral. Pathol. Oral. Radiol.*, vol. 58, pp. 589–599, 1984.

[3] S. W. Schneider, "A comparison of canal preparations in straight and curved root canals," *Oral Surg, Oral Med, Oral Pathol*. vol. 32, pp. 271–5, 1971.

[4] D. Green, "Double canals in single roots," *Oral Surg, Oral Med, Oral Pathol*. vol. 35, pp. 689–696, 1973.

[5] T. Von Arx, "Frequency and type of canal isthmuses in first molars detected by endoscopic inspection during periradicular surgery," *Int. Endod. J*., vol. 38, pp. 160–168, 2005.

[6] M. D. Fabbro and S. Taschieri, "Endodontic therapy using magnification devices: A systematic review," *J. Endodont.*, vol. 38, pp. 269–275, 2010.

[7] A. Dawood, S. Patel, and J. Brown, "Cone beam CT in dental practice," *Br. Dent. J*., vol. 207, pp. 23–28, 2009.

[8] E. Y. Sidky and X. Pan, "Image reconstruction in circular cone-beam computed tomography by constrained, total-variation minimization," *Phys. Med. Biol*., vol. 53, no. 17, pp. 4777–4807, 2008.

[9] T. P. Cotton, T. M. Geisler, D. T. Holden, S. A. Schwartz, and W. G. Schindler, "Endodontic applications of cone-beam volumetric tomography," *J. Endodont*., vol. 33, pp. 1121–1132, 2007.

[10] C. Estrela, M. R. Bueno, C. R. Leles, B. Azevedo, and J. R. Azevedo, "Accuracy of cone beam computed tomography and panoramic and periapical radiography for detection of apical periodontitis," *J. Endodont*., vol. 34, pp. 273–279, 2008.

[11] P. H. Tran, D. S. Mukai, M. Brenner, and Z. Chen, "In vivo endoscopic optical coherence tomography by use of a rotational microelectromechanical system probe," *Opt. Lett*., vol. 29, no. 11, pp.1236–1238, 2004

[12] N. Ortega-Quijano , F. Fanjul-Vélez , and J. L. Arce-Diego, "Optical crosstalk influence in fiber imaging endoscopes design," *Opt. Commun.*, vol. 283, pp.633–638, 2010.

[13] R. L. Harzic, M. Weinigel, I. Riemann, K. König, and B. Messerschmidt, "Nonlinear optical endoscope based on a compact two axes piezo scanner and a miniature objective lens," *Opt. Express*, vol. 16, pp.20588–20596 ,2008.

[14] G. J. Tearney, S. A. Boppart, B. E. Bouma, M. E. Brezinski, N. J. Weissman, J. F. Southern, and J. G. Fujimoto, "Scanning single-mode fiber optic catheter–endoscope for optical coherence tomography," *Opt. Lett.*, vol. 21, pp. 543–545, 1996.

[15] M.-A. Geibel, "Development of a new micro-endoscope for odontological application," *Eur. J. Med. Res*., vol. 11, pp. 123–127, 2006

[16] R. V. Stambaugh, G. Myers, W. Ebling, B. Beckman, and K. Stambaugh, "Endoscopic visualization of the submarginal gingiva dental sulcus and tooth root surfaces," *J. Periodontol*, vol. 73, pp. 374–82, 2002.

[17] G. W. Marshall Jr., M. R. Lipsey, M.A. Heuer, C. Kot, R. Smarz, and M. Epstein, "An endodontic fiber optic endoscope for viewing instrumented root canals," *J. Endodont*., vol. 7, pp. 85–88, 1981

[18] S. Yoshii, T. Nishino, T. Nishihara, C. Kitamura, Y. Zhang, Hao Chen, S. Ikezawa, Lev Zimin and T. Ueda, "Development of a low cost diagnostic system for dental therapy," *6th International Conference on Sensing Technology, pp. 492–496, 2015*.

[19] S. Yoshii, Y. Zhang, S. Ikezawa, C. Kitamura, T. Nishihara, and T. Ueda, "Study of endoscopy for dental treatment," *Int. J. Smart Sensing Intell. Syst.*, vol. 6, no. 1, pp. 1–17, 2013.

[20] M. Fujimoto, S. Yoshii, S. Ikezawa, T. Ueda, C. Kitamura, "Development of dental endoscope for root canal observation," *9th International Conference on Sensing Technology*, pp. 551–556, 2015.

[21] H. Kosaka, M. Kajita, Y. Li, and Y. Sugimoto, "A two-dimensional optical parallel transmission using a vertical-cavity surface-emitting laser array module and an image fiber," *IEEE Photon. Technol. Lett.*, vol. 9, no. 2, pp. 253–255, 1997

[22] X. Chen, K.L. Reichenbach, and C. Xu, "Experimental and theoretical analysis of core-to-core coupling on fiber bundle imaging, " *Opt. Express*, vol. 16, no. 26, pp. 21598–21607, 2008

[23] K. L. Reichenbach and C. Xu, "Numerical analysis of light propagation in image fibers or coherent fiber bundles, " *Opt. Express*, vol. 15, pp. 2151–2165, 2007

[24] M. Osanai, T. Suzuki, A. Tamura, T. Yonemura, and I. Mori, "Development of a micro-imaging probe for functional brain imaging," *Neurosci. Res*., vol. 75, pp. 46–52, 2013.

[25] J. Knittela, L. Schnieder, G. Buess, B. Messerschmidt, and T. Possnerb, "Endoscope-compatible confocal microscope using a gradient index-lens system," *Opt. Commun*., vol. 188, pp. 267–273, 2001.

[26] Y. Mao, S. Chang, S. Sherif, and C. Flueraru, "Graded-index fiber lens proposed for ultrasmall probes used in biomedical imaging," *Appl. Opt*., vol. 46, pp. 5887–5894, 2007.

[27] X. Li and W. Yu, "Deep tissue microscopic imaging of the kidney with a gradient-index lens system," *Biomed. Opt. Express*, vol. 4, pp. 652–658, 2013.

[28] T. Xie, S. Guo, Z. Chen, D. Mukai, and M. Brenner "GRIN lens rod based probe for endoscopic spectral domain optical coherence tomography with fast dynamic focus tracking," *Opt. Express*, vol. 14, pp. 3238–3246, 2006

[29] Li Yulin, Li Tonghai, Jiao Guohua, Hu Baowen, Huo Junmin, Wang Lili "Research on micro-optical lenses fabrication technology," *Optik - International Journal for Light and Electron Optics*, vol. 118, pp. 395–401, 2007

[30] Y. Suematsu , K. Iga ; S. Ito"A Light Beam Waveguide Using Hyperbolic-Type Gas Lenses," *IEEE Transactions on Microwave Theory and Techniques*, vol.14, Issue: 12, pp.657-665, 1966

[31] Koichi Nishizawa "Principle and Application on Gradient Index Optical Imaging," *The Review of Laser Engineering*, vol. 8, pp. 748-758, 1980.

[32] A. K. S. Braz, B. B. C. Kyotoku, R. Braz, and A. S. L. Gomes, "Evaluation of crack propagation in dental composites by optical coherence tomography," *Dent. Mater*, vol. 25, pp. 74–79, 2009.

[33] A. G. Mignani and F. Baldini, "In-vivo biomedical monitoring by fiber-optic systems," *IEEE/OSA J. Lightwave Technol*., vol. 13, no. 7, pp. 1396–1406, 1995.

[34] K-C. Huang and P. R. Wesselink, "The pulse excitation of UV LED source for fluorescence detection," *2011 IEEE Instrumentation and Measurement Technology Conference* (I2MTC), pp. 1–4, 2011.

[35] T. Hopp, P. Baltzer, M. Dietzel, W. A. Kaiser, and N. V. Ruiter, "2D/3D image fusion of X-ray mammograms with breast MRI: visualizing dynamic contrast enhancement in mammograms," *Int. J. Comput. Assist. Radiol. Surg*., vol. 7, pp. 339–348, 2012.

[36] A. S. Abdelrehim, A. A. Farag, A. M. Shalaby, and M. T. El-Melegy, "2D-PCA shape models: application to 3D reconstruction of the human teeth from a single image," *Medical Computer Vision. Large Data in Medical Imaging*, *Lecture Notes in Computer Science*, vol. 8331, pp. 44–52, 2014.

[37] A. Abdelrahim, A. Shalaby, S. Elhabian, J. Graham, and A. Farag, "A 3D reconstruction of the human jaw from a single image," *Image Processing (ICIP) 2013 20th IEEE International Conference*, pp. 3622–3626, 2013.

[38] O. A. Peters, C. I. Peters, K. Scho, and F. Barbakow, "ProTaper rotary root canal preparation: effects of canal anatomy on final shape analysed by micro CT," *Int. Endodont. J.*, vol. 36, 86–92, 2003.

[39] Y. Hirogaki, T. Sohmura, H. Satoh, J. Takahashi, and K. Takada, "Complete 3-D reconstruction of dental cast shape using perceptual grouping," *IEEE Trans. Med. Imaging*, vol. 20, pp. 1093–1101, 2001.